The Effect of Water on Gold Supported Chiral Graphene Nanoribbons: Rupture of Conjugation by an Alternating Hydrogenation Pattern

Alejandro Berdonces-Layunta, $^{*a,b,\alpha}$ Adam Matěj, $^{*c,d,e,\beta}$ Alejandro Jiménez-Martín, c,d,f James Lawrence, a,b Mohammed S. G. Mohammed, a,b Tao Wang, a,b Benjamin Mallada, c,d,e Bruno de la Torre, d Adrian Martínez, g Manuel Vilas-Varela, g Reed Nieman, h Hans Lischka, h Dana Nachtigalová, e,i Diego Peña, g Pavel Jelínek, $^{c,d,\gamma}$ and Dimas G. de Oteyza, $^{a,b,j,\delta}$

In the last few years we have observed a breakpoint in the development of graphene-derived technologies, such as liquid phase filtering and their application to electronics. In most of these cases, they imply exposure of the material to solvents and ambient moisture, either in the fabrication of the material or the final device. The present study demonstrates the sensitivity of graphene nanoribbon (GNR) zigzag edges to water, even in extremely low concentrations. We have addressed the unique reactivity of (3,1)-chiral GNR with moisture on Au(111). Water shows a reductive behaviour, hydrogenating the central carbon of the zigzag segments. By combining scanning tunnelling microscopy (STM) with simulations, we demonstrate how their reactivity reaches a thermodynamic limit when half of the unit cells are reduced, resulting in an alternating pattern of hydrogenated and pristine unit cells starting from the terminal segments. Once a quasi-perfect alternation is reached, the reaction stops regardless of the water concentration. The hydrogenated segments limit the electronic conjugation of the GNR, but the reduction can be reversed both by tip manipulation and annealing. Selective tip-induced dehydrogenation allowed to stabilize radical states on the edge of the ribbons, while the annealing of the sample completely recovered the original, pristine GNR.

1 Introduction

Since the discovery of graphene, many studies put their focus on the interaction between graphene nanostructures and water. ^{1–4}

^a Donostia International Physics Center, 20018 San Sebastián, Spain.

 $^{^{\}it b}$ Centro de Física de Materiales, 20018 San Sebastián, Spain.

 $^{^{}c}$ Institute of Physics, Czech Academy of Sciences, 16200 Prague, Czech Republic.

^d Regional Centre of Advanced Technologies and Materials, Czech Advanced Technology and Research Institute (CATRIN), Palacký University, 783 71 Olomouc, Czech Republic.

^e Department of Physical Chemistry, Faculty of Science, Palacký University, 779 00 Olomouc, Czech Republic.

f Faculty of Nuclear Sciences and Physical Engineering, Czech Technical University in Prague, Brehova 7, Prague 1 115 19, Czech Republic

g Centro Singular de Investigación en Química Biolóxica e Materiais Moleculares (CiQUS), and Departamento de Química Orgánica, Universidade de Santiago de Compostela, 15705 Santiago de Compostela, Spain.

 $^{^{}h}$ Department of Chemistry and Biochemistry, Texas Tech University, Lubbock, TX 79409-1061, USA.

ⁱ Institute of Organic Chemistry and Biochemistry, Czech Academy of Sciences, 16000 Prague, Czech Republic.

J Nanomaterials and Nanotechnology Research Center (CINN), CSIC-UNIOVI-PA, 33940 El Entrego, Spain.

 $^{^{\}alpha}$ ABerdonces95@gmail.com

β mateja@fzu.cz.

γ jelinekp@fzu.cz.

 $^{^{\}delta}$ d.g.oteyza@cinn.es.

 $^{^{}st}$ These authors contributed equally.

Some of graphene's target applications, such as filtration 5-8 or inverse osmosis, 9 require direct contact with the solvent. However, even for applications in dry media, the ability to withstand an exposure to ambient moisture is required for their scalability and industrial feasibility. 10,11 The interaction between water and nanographenes, including GNR and polycyclic aromatic hydrocarbons (PAHs), is generally assumed to be weak^{3,12-14} and dominated by London dispersive forces. ^{1,3} For this reason, bigger, more polarizable nanographenes have a stronger interaction. 1,3,4 The utmost example of a conjugated carbon lattice, graphene, appears to be immune to water's chemical attack. However, a detail slipped out of focus: most of the studies go for the bulk (the graphene surface itself) and ignore the edges 15 which, in some cases, largely determine the properties of the carbon-based materials, as occurs e.g. for porous graphene 16,17 or graphene nanoribbons (GNRs). 18-20 For this reason, we decided to test experimentally how GNRs interact with water.

GNRs display a great edge to surface ratio and optoelectronic properties with a remarkable dependence on their width and edge shape. By way of example, whereas armchair-edged ribbons are characterized by a semiconducting band structure, zigzag GNRs are metallic. 20 In order to experiment with both types of edges, we have chosen chiral (ch-)GNRs, characterized by alternating zigzag and armchair edge segments. 21,22 Note that the narrow width of the utilized chGNRs render them semiconducting 22,23 and with only a low radical character, as corroborated with calculations.²⁴ For this reason, we consider them to be in the low end with regard to the reactivity of common zigzag edges in PAHs. 25,26 In previous experiments, we already showed how these chGNRs react with molecular oxygen. 27 O2 preferentially attacks the zigzag segments, to the point of breaking the carbon backbone. However, it remains unknown how the chGNRs react with H_2O , as well as how the aromaticity of the GNR relates to their reactivity. Although the interaction between molecules and water on a metallic surface, 28,29 as well as some inorganic reactions ^{30,31} have been readily studied, to the best of our knowledge this is the first report of an organic reaction involving water directly visualized by scanning tunneling microscopy (STM).

The ribbons are grown on a clean crystal of Au(111) under ultra-high vacuum, which allows us to expose them to high purity gases in low partial pressures. In this case we used water (H_2O) , and ethanol (EtOH) for control experiments, and studied the result by means of STM. The chGNR are hydrogenated, suggesting a reducing behaviour of both species on gold surface. The resulting hydrogenation is regioselective towards the central carbon of the zigzag segments, but keeping adjacent unit cells from reacting at once. Thus, it causes an alternating pattern of hydrogenated and pristine unit cells in the exposed chGNRs, justified thermodynamically by theoretical calculations. The use of COfuncionalized probes allows for bond-resolving (BR-STM) images of the resulting hydrogenation, ^{32,33} whereas scanning tunnelling spectroscopy (STS) allows following their effect on the electronic properties. In addition, we show how we can reverse the hydrogenation either locally with the scanning probe, whereby we can create radicals on the ribbons at will, or globally with annealing treatments, whereby we return the ribbons to their pristine state.

2 Results

Multiple samples of chiral GNRs were grown following the already published recipe, 21,22,34 the quality of which was checked by means of STM/STS/BR-STM with a CO-funcionalized tip (see Figure 1a-c). A variety of exposure conditions were performed: going from pressures around 2×10^{-7} mbar to 8×10^{-7} mbar and exposure times from 1 to 2.5 hours, altogether ranging from ~ 540 to ~ 5400 Langmuir (see Supplementary figure 1-2). The sample was held at room temperature during the exposure. Control experiments with all filaments within the vacuum chamber turned off precluded their influence in the results described henceforth. In a first check it is hard to appreciate the effect of water, as the ribbons keep their mesoscopic structure (see Figure 1e). A closer look at the topography image shows a series of transversal protrusions in the central part of some unit cells (circled in green in Figure 1e), which observed with a COfunctionalized tip appear as a wider, darker central ring of the zigzag segment (marked with yellow arrows in Figure 1g). Their appearance resembles our previous observations of hydrogenated $C sp^3$ atoms in PAH. 27,35,36 The same conclusion is reached with nc-AFM measurements (Figure 1h). However, we could not rule out a C sp³ rehybridization caused by an hydroxyl functionalization either, in both cases requiring prior or concerted water disso-

In order to address the nature of the substitution on the zig-zag carbon atoms, we repeated the experiment using ethanol. The addition of an ethoxy substituent would be easily identifiable by STM as ethoxy tails on the edges of the ribbons. A new pristine sample held at room temperature was exposed to 7×10^{-8} mbar of ethanol for 20 minutes (63 Langmuir). However, the resulting ribbons displayed defects with an identical appearance as those obtained with water, proving the H as reducing agent of the ribbons to be more favourable than the introduction of $\cdot OH$ or CH₃CH₂O. Due to the lower exposure, this sample has significantly less reacted rings (see Supplementary figure 3), which accumulate on the terminal units of the GNRs, resembling other low concentration water exposures that were performed. Although the water-exposed samples exhibited additional adsorbates, their mobility even at cryogenic temperatures (see white arrows in Fig. 1e), along with the lacking chemical sensitivity of our measurements, prevented their detailed analysis and their assignment to, e.g., the remaining hydroxyl groups. Interestingly, the reduction of a unit cell prevents hydrogenation in their immediate neighbors, revealing long range effects that affect the overall kinetic or thermodynamic viability of the reaction. Upon saturation, this results in ribbons with a dominating pattern made up by hydrogenated ends and an alternation of pristine and hydrogenated unit cells towards the ribbon's interior (see Figure 1i). Exceptions to this pattern are terminal unit cells that are not hydrogenated (accounting for about 5% of the GNR ends, see Supplementary figure 4), or two neighboring unit cells that are either both hydrogenated or both pristine. Whereas the former only occurs very rarely, the latter is relatively common (marked with red arrows in Figure 1e). Representative examples of the hydrogenation pattern of ribbons and the associated exceptions are shown in Figure

2 | 1–7

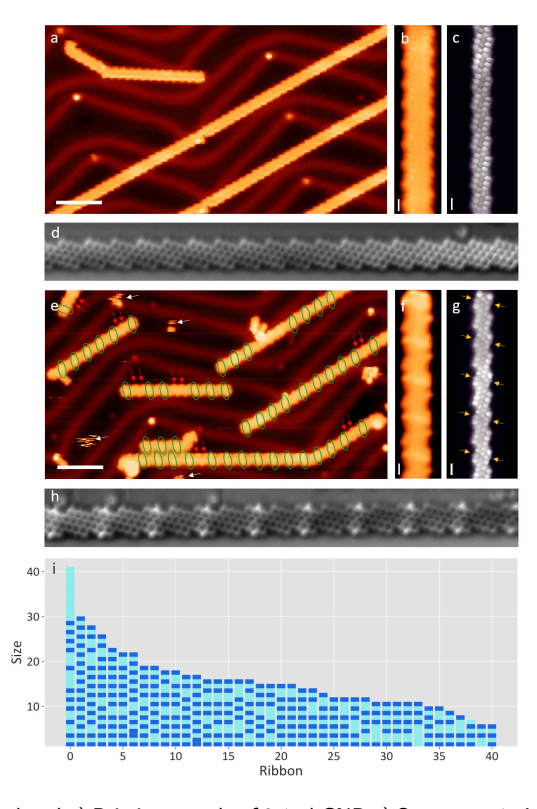


Fig. 1 a,b,c,d,e) Pristine sample of 3,1-chGNR a) Survey at -1.5V, 100pA b) Zoom on the topography c) BR-STM and d) NC-AFM image with a CO functionalized tip. e,f,g,h,i) After exposure, the ribbon zigzag edges are doubly hydrogenated in alternating unit cells. e) Survey at -1.5V, 100pA. Green circles mark hydrogenated segments, while red arrows mark consecutive pristine units. f) Zoom on the topography of a hydrogenated ribbon. g) BR-Constant height (C.H.) at 5 mV 120pA. h) NC-AFM image i) A diagram of 41 representative water-exposed ribbons from a sample exposed to 540 Langmuir of water, ordered by size, revealing the general hydrogenation pattern (not a histogram). The hydrogenated and pristine monomers are marked with dark and light blue, respectively, exhibiting their alternating pattern, along with very uncommon exceptions of two hydrogenated neighbors and the more frequently observed exceptions made up by neighboring pristine unit cells. Scale bars: a,e 5nm. b,c,d,f,g,h 5 Å

1i.

The random distribution of the defects made up by neighboring pristine unit cells hints at the following reaction dynamics: After the terminal cell has reacted, the reactive species attacks randomly any other segment of the GNR that is not next to a hydrogenated unit cell. An exposure to 560 Langmuir of water (see Figure 1e-i) is close to saturation already. Once there are no more pristine segments left that include three or more unit cells, the hydrogenation stops.

3 Theoretical insights

We employed quantum mechanical calculations to probe the thermodynamic viability of water dissociation on gold adatoms, as a way to unveil the impact of entrapped water molecules in gating hydrogenation reactions onto GNRs. We analyzed the relative binding energies of hydrogen and hydroxyl radicals (for computational details see Methods). The calculated bond dissociation energy (O-H bond) of water molecule adsorbed onto gold adatom

accounts for 81 kcal·mol $^{-1}$, thus it decreases significantly compared to the value calculated for free water (121 kcal·mol $^{-1}$) (see Supplementary figure 5). Moreover, theoretical calculations show that both hydrogen and hydroxyl radicals interact with gold adatoms with comparable binding energy (ΔE of 0.5 kcal·mol $^{-1}$). Nonetheless, the hydrogen radical binds to the zig-zag edge of GNR by 7 kcal·mol $^{-1}$ stronger compared to hydroxyl radical. The combination of water splitting plus GNR hydrogenation, whether sequential or concerted, reduces the energy balance of the reaction to reasonable levels.

The validity of such theoretical description clearly depends on the level of computation and methods used in the study. The ribbons are prone to exhibit multireference character ^{23,24}, a factor that introduces errors in the DFT calculated energies. Multireference methods, while limited to small size systems, can be used to obtain more accurate results. For this reason, we performed multireference average quadratic coupled cluster (MR-AQCC) calculations on dimer and trimer to corroborate the less computationally demanding DFT analysis. It has been shown in previous calculations, e.g. for oligoacenes³⁷ and diindenoacenes³⁸ that this method provides a balanced description of the biradicaloid and higher radicaloid character in PAHs. The calculated energy trends for both methods are found to correlate well to each other (see Supplementary figure 6). One can see that the largest error occurs for the first hydrogenation step. This fact is not surprising as addition of odd number of hydrogen radicals results in a radical structure, which can be together with the GNR's length difficult to correctly describe by DFT. Herein we focus on the thermodynamically stable products instead of the kinetics, presenting only the energetics of fully hydrogenated units. Such structures are described by DFT methods sufficiently well. Therefore, we carried out extensive DFT calculations for the relative energies and aromaticity of longer chains, from the dimer to the heptamer. The energetic trends associated to the hydrogenation reaction steps are found similar, irrespective of different chain lengths; the computational results for heptamers are presented herein as the system is capable to describe better the variety of possibilities in hydrogenation. The results obtained from the computed relative energies of partially hydrogenated GNRs are shown in Figure 2. The most stable structure calculated in the first reaction step contains the terminal unit in reduced form; here, central sp2 carbon atoms of the zigzag edge have reacted with H atoms, and such process is highlighted in Figure 2a by a black arrow. The relative energies of the products calculated after completion of the first and second (Figure 2b) step underline the proclivity towards reduction of terminal units versus the inner carbon domains of GNR. These findings agree well with the experimentally observed products, where the ending portion of the GNRs are found reduced in most cases. Further hydrogenation exhibits a clear opposition to attack subsequent units as seen in Figure 2b-d. We calculated the diradical character of GNR with increasing length as a possible mechanism for hydrogenation protection. The calculated values are summarised in Supplementary table 1 and show a saturation of diradical character y_0 around 18 %, making the studied GNR a relatively weak diradicaloid. It can be seen that the diradical character of GNR can be connected to the measured bandgap of the

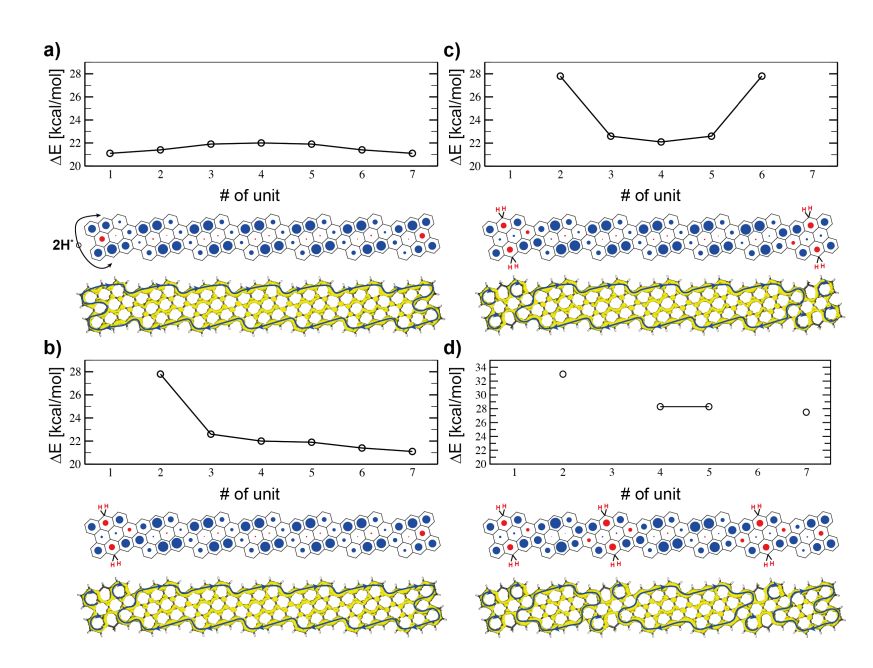


Fig. 2 Relative energies of water splitting plus hydrogenation of GNRs in different positions and level of reduction (see Methods). Addition of two H radicals to units in different positions for pristine GNR (a), GNR with one terminal unit reduced (b), GNR with both termini reduced (c) and a heptamer GNR with three reduced units as a possible final product (d). Positions of units correspond with structures below the graphs. NICS and ACID plots for each structure are shown below corresponding graphs. Blue and red circles display aromatic and antiaromatic rings, respectively. ACID isosurfaces are plotted at isovalue of 0.05 a.u.; for high-resolution see SI.

GNR (see Figure 3a), i.e., longer GNRs have small bandgaps and higher y_0 while a pristine monomer shows the largest bandgap and almost negligible y_0 . Although the diradical character on its own is not sufficient to explain the observed protection of consecutive units against hydrogenation, it offers an explanation of the stability of the final quasi-perfect alternation pattern. The diradical character drops for a pristine monomer within a GNR to a value of around 4 %, which appears to be below the threshold for successful hydrogenation in presence of water. A deeper study of the reaction mechanism and kinetics is beyond the scope of this work as the number of possible mechanisms renders such a study highly convoluted. However, the results from the relative total energies of hydrogenated products correlate well with the experimentally observed products and thus suggest that the hydrogenation caused by water exposure is thermodynamically driven.

To further investigate the reason for the observed higher stability of the alternating pattern, we carried out nucleus-independent chemical shift 39,40 (NICS) and anisotropy of induced-current density 41 (ACID) calculations in order to analyze the electronic differences between various hydrogenated products. While NICS values characterize each ring by the amount of magnetic shielding (deshielding) due to aromaticity (antiaromaticity) of that ring, another method should always be included in order to characterize the global properties of the system. The $\pi\text{-ACID}$ method offers visualization of conjugation in molecules allowing for global aromaticity description. Plots in Figure 2 show ACID and NICS results on heptamer GNRs in various stages of hydrogenation (for high resolution ACID plots on trimers see Supplementary figures 7-11, NICS of hexamers in Supplementary figure 12). The results show a globally conjugated circuit along the periphery of

the ribbon exhibiting diatropic current, proving global aromatic character of the pristine GNR together with Hückel's 4n+2 rule along the circuit. At the terminal units, the conjugation forms local antiaromatic bays, which effectively prolong the conjugated circuit by four more carbons. Although this increased conjugation path does not affect Hückel's rule, the presence of this antiaromatic bay may be responsible for the higher local reactivity of the terminal units. This effect must thus be compensated by a more stable global structure, hinting at an energetic preference for longer conjugation paths. The antiaromatic (aromatic) rings are illustrated by red (blue) circles in NICS plots with diameter proportional to the magnetic shielding magnitude. Once a unit is reduced, the conjugation changes dramatically depending on the position of the reduced unit. In all cases, the hydrogenation of a unit breaks the global conjugation through this unit, which leads to fragmentation of the periphery conjugation path. It can be seen that the pristine units extend their conjugation path towards the reduced unit by including one of its formed Clar's sextets ((see Supplementary figure 13)). When the terminus is reduced, there is a globally conjugated periphery of pristine units and three isolated benzene rings in the reduced unit cell. By reducing an internal unit cell, two conjugated paths are formed and only two isolated benzene rings form (see Figure 2d, Supplementary figure 9 and 12c,e). By considering reduction of two consecutive unit cells, four extra isolated benzene rings are formed (Supplementary figure 10, 12d,e and 13). Both calculations and experiment agree that this scenario, forming less conjugated parts (localized Clar sextets) between two consecutive hydrogenated unit cells, is energetically unfavorable. We thus infer that longer and less fragmented conjugation paths are favored.

4 | 1–7

4 Discussion

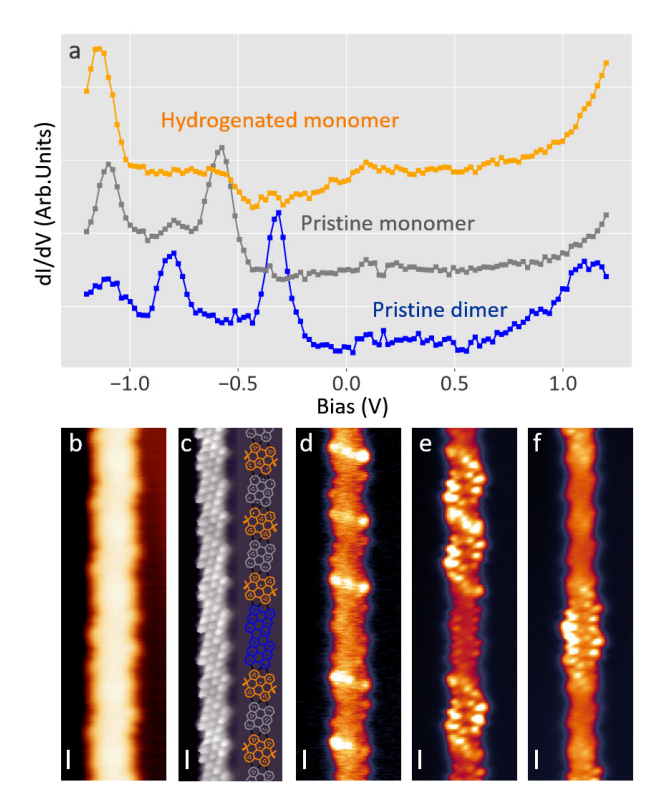


Fig. 3 Analogous images of a ribbon with alternating hydrogenated cells and a pristine dimer with a CO tip. A) Spectroscopy of the different sections of the ribbon. It shows how the hydrogenation disrupts the conjugation and increases the bandgap. B) Topography. C.C. -800mV, @50pA. C) BR C.H. 10mV at \$\tilde{2}60pA\$. Hydrogenated carbons are visible in the left edge of this backwards scan. D) dI/dV at the HOMO of the hydrogenated segments. -1.0 V, C.H. E) dI/dV at the HOMO of the pristine monomers. -600 mV, C.H. F)dI/dV at the HOMO of the pristine dimer. -350mV, C.H. Scale bars 5 Å

Hydrogenation of the two edges of a unit cell localizes the aromaticity in the contiguous aromatic rings (see Figure 2 and supplementary 8-12). The resulting structure has thus a lower conjugation and hence a wider bandgap. We performed a series of STS measurements to characterize the electronic structure of the hydrogenated graphene nanoribbons (see Figure 3a). From the spectroscopy we can observe how the HOMO of the alternating structure appears at an energy around -0.6 eV. Compared to the -0.25 eV valence band onset of the pristine ribbons, ²² this means a large increase of the ribbon's bandgap, specially considering that the LUMO also shifts from around 0.5 eV beyond 1.1 eV, which corresponds to the stability threshold of the hydrogenated ribbons (as will be shown below, higher bias dehydrogenates the ribbons back to their pristine form). The bandgap rapidly decreases if larger pristine segments are present. In the case of pristine dimers, we can observe both in the spectroscopy and in the differential conductance images how the HOMO appears at -0.3 eV, and the LUMO around 0.7 eV, implying a bandgap of around 1 eV. That is readily much closer to the 0.7 eV bandgap of longer ribbons. 22

Further efforts of measuring the LUMO of the hydrogenated

ribbons resulted in the tip-induced dehydrogenation of the ribbons. Figure 4a shows an example of how acquiring a spectrum from 0 to +1.5 eV at the position of the lightning icon causes the dehydrogenation of the C sp³ under the tip and its associated sp² rehybridization. Subsequent bond resolving STM images at low bias display greatly enhanced signal at those positions (Figure 4b). Conductance spectra show the appearance of a state around the Fermi level (Figure 4e) at this position that was previously absent. This new state is univocally identified as an unpaired electronic state, or in other terms, a radical. The remaining sp³ carbon on the opposite side of the unit cell causes an imbalance of pz electrons between the two carbon sublattices, as has been reported previously by our group with oxygen funcionalized ribbons. ^{27,35} However, whereas with oxygen-functionalized ribbons the radical state remained occupied and resulted in a net spinmoment, in these pure hydrocarbon ribbons the orbitals lie at higher energies (slightly above the substrate's Fermi level). This causes that the unpaired electron is transferred from the ribbon to the underlying Au and thereby depopulates the radical state. Nevertheless, these radical structures reveal a limited stability, and numerous attempts of getting close-by radicals on these ribbons result in the successive full dehydrogenation of the unit cells, regenerating the pristine ribbon.

The hydrogenation caused by water is thus a mild modification process of the graphene nanoribbons. Annealing the sample to 150 °C results in their complete dehydrogenation, recovering the initial sample. The electronic and molecular integrity of the recovered ribbons was confirmed. The recovery is an analogous process of the original planarization of the GNR, but for two extra factors that help the recovery: first, the ribbons are now fully planar but for this edge carbons, so the steric hindrance favours the dehydrogenation. Second, the π network environment of this edge carbon energetically stabilizes the sp² carbon of the product. ²⁶

We consider that both for the hydrogenation and the regeneration, the catalytic effect of the gold surface was influential in the process. However, most of the device preparation processes involve exposing the metal-supported ribbons to solvents for the transfer process. Not to forget either that these nanographenes have a low open shell character (from 4 % in the monomer to only about 18% in long ribbons). Wider ribbons or longer zigzag segments in GNRs of different chirality ^{23,26} will have a higher radical character and reactivity. We consider that the phenomena shown in this work are influential for the future applicability of the GNRs, and different protection strategies have to be considered in order to keep the integrity of the ribbons.

5 Conclusions

We have proved the sensitivity of (3,1,4)-chGNR on Au(111) to humidity at room temperature. Low pressure exposures of high purity water readily affected the ribbons. Control experiments with ethanol revealed that both water and ethanol split their O-H bond, promoted by the metallic surface, and hydrogenate the central carbon atom of the zigzag edges. The regioselectivity stems from the increased radical character at those positions. The hydrogenation avoids contiguous units, causing an alternating hy-

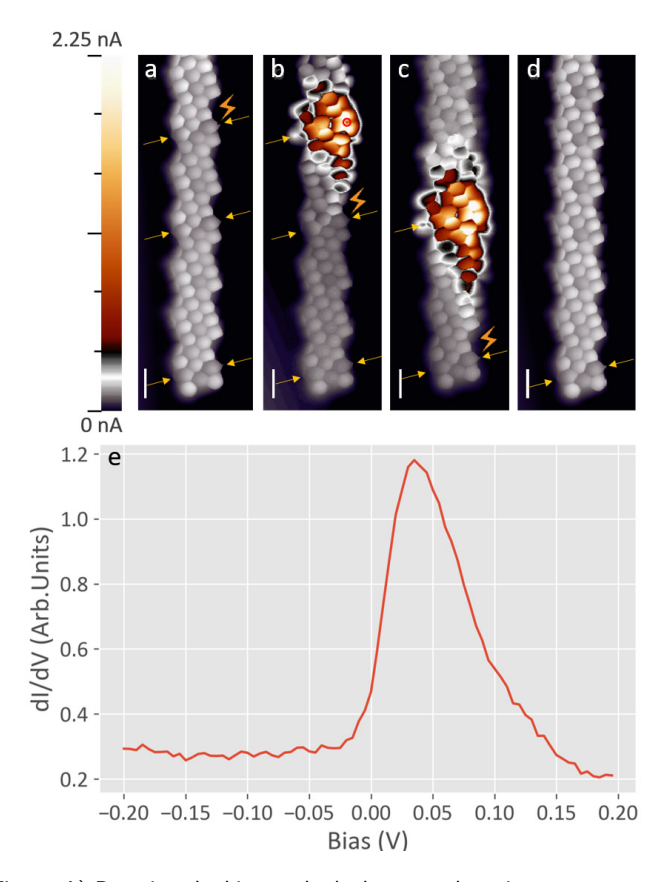


Fig. 4 A) Ramping the bias at the hydrogenated sections can promote the dehydrogenation. B) What is left is a unpaired state, stabilized by the hydrogen on the other side of the ribbon, which looks like a burst in the current around Fermi level. C) Successive bias ramps can cause successive dehydrogenations, where the radical-stabilizing hydrogen is always more likely to abstract. The result is the recovery of the D) pristine structure. Scale bars 5 Å. E) Low bias spectra at B) red spot.

drogenation pattern that typically starts from the terminal units. The double hydrogenation breaks the continuous conjugation of the ribbon and opens the bandgap in the affected sections. However, the hydrogenation process can be easily reverted by annealing treatments or by tip-induced manipulation, which further allows dehydrogenating only one side of a unit cell and thereby creating radical states at predefined positions.

Author Contributions

Alejandro Berdonces-Layunta - Experimental investigation, formal analysis of the experimental data, visualization and writing of the original manuscript.

Adam Matěj - Theoretical investigation, formal analysis of the theoretical data, visualization and writing of the original manuscript.

James Lawrence - Experimental investigation, review and editing.

Mohammed S. G. Mohammed - Experimental investigation. Tao Wang - Experimental investigation, review and editing. Benjamin Mallada, Bruno de la Torre, Alejandro Jiménez Martín - Experimental investigation (NC-AFM images)

Adrian Martínez - Resources, synthesis of the molecular precur-

sors.

Manuel Vilas-Varela - Methodology for the precursors employed.

Reed Nieman - Theoretical investigation

Hans Lischka - Methodology, supervision.

Dana Nachtigalova - Theoretical investigation.

Diego Peña - Methodology for the precursors, supervision.

Pavel Jelínek - Resources, supervision, methodology, project administration and review and editing of the article.

Dimas G. De Oteyza - Resources, conceptualization, supervision, methodology, project administration and review and editing of the article.

Conflicts of interest

There are no conflicts to declare.

Acknowledgement

We acknowledge financial support from MCIN/AEI/10.13039/501100011033 (grant nos. PID2019-107338RB-C62, PID2019-107338RB-C63,PID2022-140845OB-C64) and the European Union "NextGenerationEU"/PRTR (TED2021-132388B-C43); the European Union's Horizon 2020 research and innovation program (grant no. 863098 and Marie Skłodowska-Curie Actions Individual Fellowship No. 101022150), the Xunta de Galicia (Centro Singular de Investigación de Galicia, 2019-2022, grant no.

P.J. and A.M. acknowledge support of Praemium Academie of the Academy of Science of the Czech Republic and Czech Science Foundation projects no. 20-13692X. We acknowledge computational resources provided by the project "e-Infrastruktura CZ" (e-INFRA CZ LM2018140) supported by MEYS CR. A.M. thanks for support from Internal Student Grant Agency of the Palacký University in Olomouc, Czech Republic, IGA_PrF_2023_018 and the Endowment Fund of the Palacký University in Olomouc, Czech Republic. H.L. wants to acknowledge support by the National Science Foundation [grant number 2107923], Division of Chemistry.

Notes and references

- 1 E. M. Cabaleiro-Lago, J. A. Carrazana-García and J. Rodríguez-Otero, *The Journal of Chemical Physics*, 2009, **130**, 234307.
- 2 S. Tsuzuki and T. Uchimaru, *Current Organic Chemistry*, 2006, **10**, 745–762.
- D. Feller and K. D. Jordan, *The Journal of Physical Chemistry* A, 2000, 104, 9971–9975.
- 4 C. S. Lin, R. Q. Zhang, S. T. Lee, M. Elstner, T. Frauenheim and L. J. Wan, *The Journal of Physical Chemistry B*, 2005, **109**, 14183–14188.
- 5 S. Blankenburg, M. Bieri, R. Fasel, K. Müllen, C. A. Pignedoli and D. Passerone, *Small*, 2010, **6**, 2266–2271.
- 6 J. Ma, M. Yang, F. Yu and J. Zheng, Scientific Reports, 2015, 5, 13578.
- 7 Y. Yang, X. Yang, L. Liang, Y. Gao, H. Cheng, X. Li, M. Zou, R. Ma, Q. Yuan and X. Duan, *Science*, 2019, 364, 1057–1062.

6 | 1–7

- 8 R. R. Nair, H. A. Wu, P. N. Jayaram, I. V. Grigorieva and A. K. Geim, *Science*, 2012, **335**, 442–444.
- 9 D. Cohen-Tanugi and J. C. Grossman, *Nano Letters*, 2012, **12**, 3602–3608.
- 10 S. Han, D. Wu, S. Li, F. Zhang and X. Feng, Advanced Materials, 2014, 26, 849–864.
- 11 P. R. Kidambi, D. D. Mariappan, N. T. Dee, A. Vyatskikh, S. Zhang, R. Karnik and A. J. Hart, ACS Applied Materials & Interfaces, 2018, 10, 10369–10378.
- 12 H. Li and X. C. Zeng, ACS Nano, 2012, 6, 2401–2409.
- 13 O. Leenaerts, B. Partoens and F. M. Peeters, *Physical Review B*, 2009, **79**, 235440.
- 14 G. Hong, Y. Han, T. M. Schutzius, Y. Wang, Y. Pan, M. Hu, J. Jie, C. S. Sharma, U. Müller and D. Poulikakos, *Nano Letters*, 2016, 16, 4447–4453.
- 15 A. H. Holm, R. Møller, K. H. Vase, M. Dong, K. Norrman, F. Besenbacher, S. U. Pedersen and K. Daasbjerg, New Journal of Chemistry, 2005, 29, 659.
- 16 Z. Mutlu, P. H. Jacobse, R. D. McCurdy, J. P. Llinas, Y. Lin, G. C. Veber, F. R. Fischer, M. F. Crommie and J. Bokor, Advanced Functional Materials, 2021, 31, 2103798.
- 17 C. Moreno, M. Vilas-Varela, B. Kretz, A. Garcia-Lekue, M. V. Costache, M. Paradinas, M. Panighel, G. Ceballos, S. O. Valenzuela, D. Peña and A. Mugarza, *Science*, 2018, 360, 199–203.
- 18 Z. Mutlu, J. P. Llinas, P. H. Jacobse, I. Piskun, R. Blackwell, M. F. Crommie, F. R. Fischer and J. Bokor, ACS Nano, 2021, 15, 2635–2642.
- 19 J. Cai, P. Ruffieux, R. Jaafar, M. Bieri, T. Braun, S. Blankenburg, M. Muoth, A. P. Seitsonen, M. Saleh, X. Feng, K. Müllen and R. Fasel, *Nature*, 2010, **466**, 470–473.
- 20 M. Corso, E. Carbonell-Sanromà and D. G. de Oteyza, *On-Surface Synthesis II*, Springer International Publishing, Cham, 2018, pp. 113–152.
- 21 D. G. de Oteyza, A. García-Lekue, M. Vilas-Varela, N. Merino-Díez, E. Carbonell-Sanromà, M. Corso, G. Vasseur, C. Rogero, E. Guitián, J. I. Pascual, J. E. Ortega, Y. Wakayama and D. Peña, ACS Nano, 2016, 10, 9000–9008.
- 22 N. Merino-Díez, J. Li, A. Garcia-Lekue, G. Vasseur, M. Vilas-Varela, E. Carbonell-Sanromà, M. Corso, J. E. Ortega, D. Peña, J. I. Pascual and D. G. de Oteyza, *The Journal of Physical Chemistry Letters*, 2018, 9, 25–30.
- 23 J. Li, S. Sanz, N. Merino-Díez, M. Vilas-Varela, A. Garcia-Lekue, M. Corso, D. G. de Oteyza, T. Frederiksen, D. Peña and J. I. Pascual, *Nature Communications*, 2021, **12**, 5538.
- 24 A. Konishi and T. Kubo, *Topics in Current Chemistry*, 2017, 375, 83.

- 25 E. F. Sheka and L. A. Chernozatonskii, *International Journal of Quantum Chemistry*, 2009, NA–NA.
- 26 D.-e. Jiang, B. G. Sumpter and S. Dai, *The Journal of Chemical Physics*, 2007, **126**, 134701.
- 27 A. Berdonces-Layunta, J. Lawrence, S. Edalatmanesh, J. Castro-Esteban, T. Wang, M. S. G. Mohammed, L. Colazzo, D. Peña and P. Jelínek, ACS Nano, 2021, 8.
- 28 K. Lucht, D. Loose, M. Ruschmeier, V. Strotkötter, G. Dyker and K. Morgenstern, *Angewandte Chemie International Edition*, 2018, **57**, 1266–1270.
- 29 K. Lucht, I. Trosien, W. Sander and K. Morgenstern, *Angewandte Chemie International Edition*, 2018, **57**, 16334–16338.
- 30 H. Shi, H. Yuan, Y. Sun, X. Ma, Z. Li, D. Zhou, Z. Li and X. Shao, *Nano Letters*, 2021, **21**, 9567–9572.
- 31 O. Bikondoa, C. L. Pang, R. Ithnin, C. A. Muryn, H. Onishi and G. Thornton, *Nature Materials*, 2006, **5**, 189–192.
- 32 D. G. de Oteyza, P. Gorman, Y.-C. Chen, S. Wickenburg, A. Riss, D. J. Mowbray, G. Etkin, Z. Pedramrazi, H.-Z. Tsai, A. Rubio, M. F. Crommie and F. R. Fischer, *Science*, 2013, 340, 1434–1437.
- 33 L. Gross, F. Mohn, N. Moll, P. Liljeroth and G. Meyer, *Science*, 2009, **325**, 1110–1114.
- 34 N. Merino-Díez, M. S. G. Mohammed, J. Castro-Esteban, L. Colazzo, A. Berdonces-Layunta, J. Lawrence, J. I. Pascual, D. G. de Oteyza and D. Peña, *Chemical Science*, 2020, 11, 5441–5446.
- 35 T. Wang, S. Sanz, J. Castro-Esteban, J. Lawrence, A. Berdonces-Layunta, M. S. G. Mohammed, M. Vilas-Varela, M. Corso, D. Peña, T. Frederiksen and D. G. de Oteyza, *Nano Letters*, 2022, 22, 164–171.
- 36 J. Holec, B. Cogliati, J. Lawrence, A. Berdonces-Layunta, P. Herrero, Y. Nagata, M. Banasiewicz, B. Kozankiewicz, M. Corso, D. G. Oteyza, A. Jancarik and A. Gourdon, *Angewandte Chemie International Edition*, 2021, **60**, 7752–7758.
- 37 F. Plasser, H. Pašalić, M. H. Gerzabek, F. Libisch, R. Reiter, J. Burgdörfer, T. Müller, R. Shepard and H. Lischka, *Angewandte Chemie International Edition*, 2013, **52**, 2581–2584.
- 38 R. Nieman, N. J. Silva, A. J. A. Aquino, M. M. Haley and H. Lischka, *The Journal of Organic Chemistry*, 2020, **85**, 3664–3675.
- 39 P. v. R. Schleyer, C. Maerker, A. Dransfeld, H. Jiao and N. J. R. van Eikema Hommes, *Journal of the American Chemical Society*, 1996, **118**, 6317–6318.
- 40 D. Geuenich, K. Hess, F. Köhler and R. Herges, *Chemical Reviews*, 2005, **105**, 3758–3772.
- 41 R. Herges and D. Geuenich, *The Journal of Physical Chemistry A*, 2001, **105**, 3214–3220.